Microstructural and Magnetic Behavior of Nanocrystalline Fe-12Ni-16B-2Si Alloy Synthesis and Characterization

Kaouther Zaara [1], **Mohamed Khitouni** [2], **Lluisa Escoda** [1], **Joan Saurina** [1], **Joan-Josep Suñol** [1,*], **Nuria Llorca-Isern** [3] and **Mahmoud Chemingui** [2]

[1] Department of Physics, University of Girona, 17003 Girona, Spain; kaouther_zaara@hotmail.fr (K.Z.); lluisa.escoda@udg.edu (L.E.); joan.saurina@udg.edu (J.S.)

[2] Laboratoy of Inorganic Chemistry, Faculty of Sciences, University of Sfax, Sfax 3018, Tunisia; mohamed.khitouni@fss.rnu.tn (M.K.); mahmoud.chminghi@fss.rnu.tn (M.C.)

[3] Department CMEM, University of Barcelona, 08028 Barcelona, Spain; nullorca@ub.edu

[*] Correspondence: joanjosep.sunyol@udg.edu; Tel.: +34-972-419-757

Abstract: The nanocrystalline $Fe_{70}Ni_{12}B_{16}Si_2$ (at.%) alloy was prepared by mechanical alloying (MA) of elemental powders in a high-energy planetary ball mill. Phase evolution, microstructure, thermal behavior and magnetic properties were investigated. It was found that a body-centered cubic structured solid solution started to form after 25 h milling and a faced-centered cubic structure solid solution started to form after 50 h of milling; its amount increased gradually with increasing milling time. The BCC and the FCC phases coexisted after 150 h of milling, with a refined microstructure of 13 nm and a 10 nm crystallite size. The as-milled powder was annealed at 450 °C and 650 °C and then investigated by vibrating sample magnetometry (VSM). It was shown that the semi-hard magnetic properties are affected by the phase transformation on annealing. The saturation magnetization decreases after annealing at 450 °C, whereas annealing at 650 °C improves the magnetic properties of 150 h milled powders through the reduction of coercivity from 109 Oe to 70 Oe and the increase in saturation magnetization.

Keywords: ball milling; X-ray diffraction; nanocrystalline; semi-hard; thermal stability

1. Introduction

In recent years, Iron-Nickel alloys have attracted considerable attention in both applied and fundamental science. They are widely used in industrial applications due to their soft magnetic properties, such as narrow hysteresis loops, small magnetic losses and low coercive fields [1,2]. Various methods were used to synthesize FeNi-based nanomaterials, including electrodeposition, rapid solidification, plasma reaction of metal, thermal evaporation and mechanical alloying [3]. The mechanical alloying (MA) technique offers a low cost of installation, easy control of the process parameters, and production of materials with various mechanical properties [4,5]. It has been reported that the addition of other elements to the binary Fe-Ni alloy system is usually followed by significant modifications in terms of microstructural, structural, mechanical, magnetic and other properties. Accordingly, the mechanical alloying of the Fe-Ni-based alloys has been the subject of a number of studies, including those focused on Fe-Ni-Cu [6,7], Fe-Ni-Cr [8], Fe-Ni-Co [9], Fe-Ni-Zr-B [10] and Fe-Ni-Co-Ti-B [11]. However, there are few published works concerning production by mechanical alloying of the quaternary Fe-Ni-B-Si powders [12–15].

In the present study, the Fe-Ni-B-Si alloy, with a new composition as $Fe_{70}Ni_{12}B_{16}Si_2$ alloy, was produced by the mechanical alloying process. It is known that the magnetic behavior is better if the percentage of the magnetic elements (Fe and Ni in this study) is around 83 at.% [16]. Likewise, high B/Si ratio is associated with a lower reduction of the saturation magnetic flux density (if compared with low B/Si ratio alloys) [17]. We studied the influence of milling time on morphology, phase evolution, and the structure

and microstructure of the powders. In addition, we investigated the thermal behavior and the influence of heat treatment on structural, microstructural and magnetic properties of the as-milled powders.

2. Materials and Methods

Elemental powders (Sigma Aldrich, Saint Louis, MO, USA) of Fe (99.7 at.% purity, 30 μm grain size), Ni (99.7%, <30 μm), Si (99.9%, <45 μm) and amorphous B (10 μm, 99.6%) were mechanically alloyed in argon atmosphere to produce a nominal composition of $Fe_{70}Ni_{12}B_{16}Si_2$ alloy by using the high energy planetary ball mill technique (Pulverized P7, Fritsch, Idar-Oberstein, Germany) at a speed of 600 rpm, with a ball-to-powder weight ratio about 15:1. The milling sequence was chosen such as 10 min of milling followed by 5 min of pause, to avoid powder agglomeration and sticking of the powder to container walls and balls. The initial powders were milled for 1, 5, 10, 25, 50, 80, 100, 125 and 150 h. The phase identification and the structural evolution were investigated by X-ray diffraction (XRD) by means of D-500 S equipment (Bruker, Billerica, MA, USA) with Cu Kα (λ = 1.5406 Å) radiation. The structural parameters were obtained from the Rietveld refinement of the XRD patterns by the Maud program (Maud, Trento, Italy) [18,19]. The morphology of the milled powder was examined using scanning electron microscopy (SEM) with a DSM960A ZEISS microscope (Carl Zeiss GmbH, Jena, Germany) in secondary electron mode operating at a voltage of 15 kV, coupled with energy-dispersive X-Ray spectroscopy (EDS) microanalysis. Differential scanning calorimetry (DSC) was performed using DSC822 equipment (Mettler-Toledo, Columbus, OH, USA) under argon atmosphere, in the temperature range from 200 °C to 700 °C, at a heating rate of 20 °C min^{-1}. The 150 h milled powder was annealed in sealed quartz tubes evacuated to 10^{-3} under argon atmosphere for 1 h at 450 °C and 650 °C. Annealing was performed in an oven, with a heating rate of 15 °C/min. The magnetic characterization of the as-milled and heat-treated powders was conducted by a superconducting quantum interference SQUID MPMS-XL device (Quantum Design; San Diego, CA, USA) at 300 K, with a maximum applied field of 20 kOe.

3. Results and Discussion

3.1. Powder Morphology

Figure 1 shows the morphology evolution of the powder milled for different times. Before milling, the powder particles have a random size, as seen in Figure 1a. After 5 h of milling, the particles become larger, with irregular shape and size due to the agglomeration and cold welding. Both phenomena are clearly seen at this stage (Figure 1b). After 25 h of milling, the flattening of the particle size is observed due to the introduction of compressive forces into the particles, introduced by successive collisions (Figure 1c). After 50 h, the majority of particles became smaller. However, large particles can be seen (Figure 1d). Increasing milling time to 100 h and 150 h results in a high uniformity and straight distribution of particle sizes, so a steady state was noticed (Figure 1e,f). The presence of some agglomerated particles can be explained by the prolonged milling time. EDS microanalysis confirms that contamination from milling tools is lower than 1 at.%.

3.2. Microstructural Analysis

XRD patterns of all compounds were analyzed using Maud software (version 2.55), based on the Rietveld powder structure refinement method [20,21]. In order to check the functional behavior of these alloys, it is necessary to obtain good refinements to stabilize the microstructure. The ratio of reliability parameters, represented as GoF (goodness of fit = R_{wp}/R_{exp}), gives information about the quality of fit, where R_{wp} and R_{exp} are the weighted residual error and the expected error, respectively [19,22]. The best refinement is reached when GoF approaches 1.0 (Table 1).
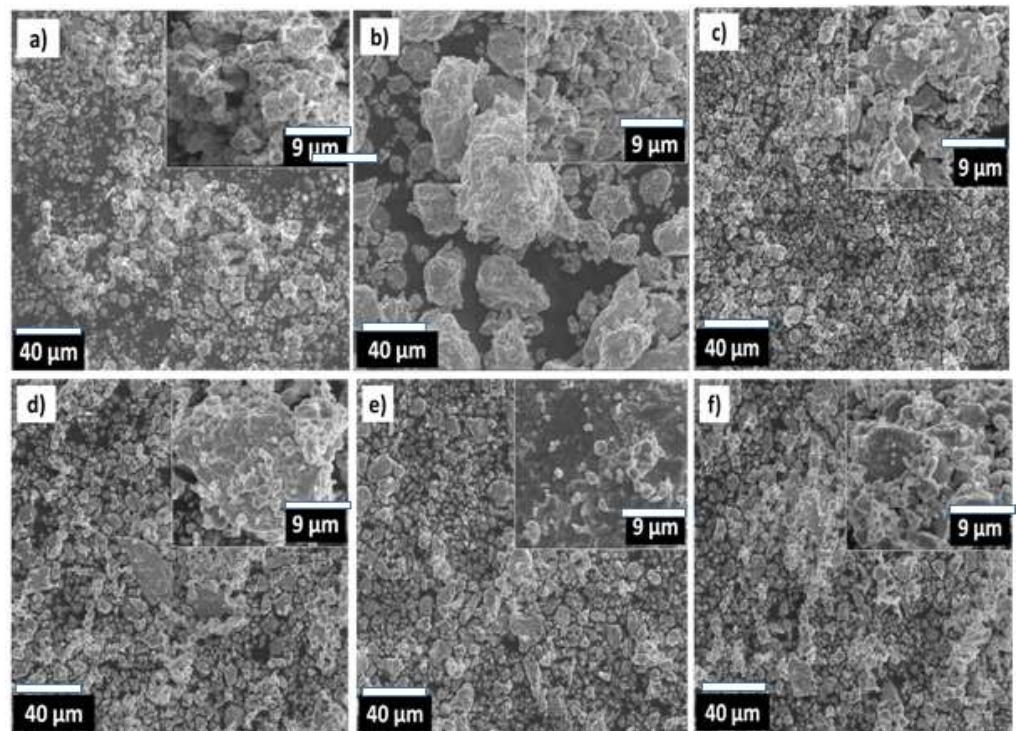
Figure 1. Scanning electron micrographs corresponding to mechanically milled powders: (**a**) 0 h, (**b**) 5 h, (**c**) 25 h, (**d**) 50 h, (**e**) 100 h and (**f**) 150 h. The bar scale of the images (except inserts: 9 μm) is 40 μm.

Table 1. Residual parameters and GoF values of the compounds revealed from Rietveld analysis.

Milling Time (h)	R_{wp}	R_{exp}	GoF (R_{wp}/R_{exp})
0	3.82	2.95	1.29
1	3.53	3.23	1.09
5	2.49	2.19	1.13
10	2.38	2.20	1.08
25	2.24	1.91	1.17
50	2.30	2.11	1.08
80	2.39	2.07	1.15
100	2.45	2.12	1.15
125	2.38	2.14	1.11
150	2.37	2.17	1.09

Figure 2 shows the X-ray diffraction patterns of the powders at various milling times. The unmilled powder blends (0 h) show the existence of the characteristic peaks of the three pure elements' crystalline structures: BCC-Fe, FCC-Ni and FCC-Si. The B phase diffraction cannot be observed because of its amorphous state and its low atomic scattering factor. The reduced intensity of Si peaks is due to its low atomic number and to its small percentage in comparison with those of Ni and Fe (Figure 3a). After milling for 1 h, elemental iron, nickel and silicon were detected by XRD. One can see a decrease of all peak intensities and the broadening of nickel and iron peaks. The iron peak profile becomes asymmetric. This could be explained by the diffusion of B atoms into the iron lattice, resulting in the formation of a BCC Fe (B) solid solution (Figure 3b). The enthalpy of formation of this phase is approximately ($\Delta H = -35$ kJ/mol), as listed in Table 2. It should be noted that during the severe plastic deformation, boron atoms can be diffused in the interstitial sites of the iron matrix [23]. After 5 h of milling, all silicon peaks vanished. and iron peaks became broadened and asymmetric, indicating that a supersaturated BCC Fe (B, Si) solid solution was achieved (Figure 3c). Regarding the shape of the Ni peak, its width increases with milling time, suggesting a decrease in the crystallite size. However, we do not notice

a significant asymmetry or shift of the Ni peak toward lower angles. As a result, we are unable to assume remarkable alloy element dissolution in the Ni lattice during the first 25 h of milling.
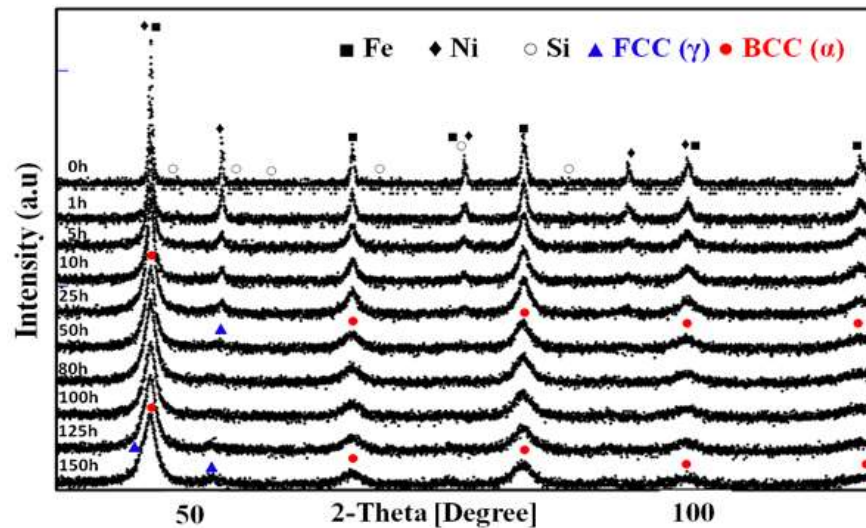

Figure 2. X-ray diffraction patterns of $Fe_{70}Ni_{12}B_{16}Si_2$ powders as a function of mechanical alloying time.

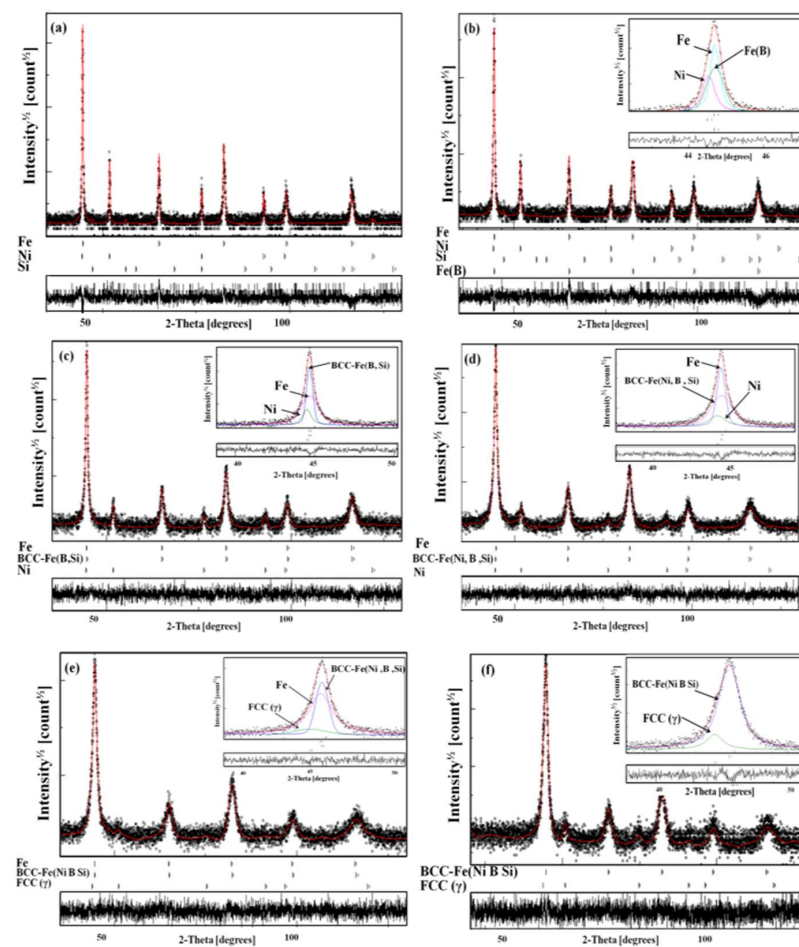**Figure 3.** Rietveld refinement of the XRD pattern of the $Fe_{70}Ni_{12}B_{16}Si_2$ powder (**a**) before milling and after (**b**) 1 h, (**c**) 5 h, (**d**) 25 h, (**e**) 50 h and (**f**) 150 h. The peak (110) fitted with the pseudo-Voigt function is shown in the insert.

After 25 h of milling, the Fe diffraction peak profiles become more asymmetric and broaden. These phenomena demonstrate that Ni gradually reacts with Fe (B, Si) to form a disordered solid solution BCC-Fe (Ni, B, Si) (BCC (α) phase, Fe rich) (Figure 3d). Since there is no remarkable shift or asymmetry in the Ni peak, we exclude the diffusion of Fe, B and Si atoms in the Ni lattice. Thus, the interdiffusion of Fe and Ni cannot occur during the first 25 h of milling. Previously, the absence of interdiffusion between Fe and Ni was reported in some works [24–27]. The alloying process in this study results from the relatively high negative heat of mixing between the initial elements (Table 2) [28]. Moreover, during the MA process, different factors such as temperature of powders, density of defects (like vacancies and dislocations) and reduced crystalline size can affect the diffusion process [29]. The formation of disordered solid solutions, FCC and BCC lattice, are formed after 50 h of milling, due to an obvious shift of the FCC Ni peak position [30], and the α-Fe has smaller 2θ angles (Figure 3e). Therefore, dissolution of the alloy elements into the Ni lattice is deduced at this stage of milling. The disordered structures of the FCC and BCC solid solutions of the $Fe_{70}Ni_{12}B_{16}Si_2$ alloy mean that Fe, Ni, B and Si atoms occupy the FCC and BCC lattice sites randomly.

During milling, the increase in the line broadening is due to the reduction in crystallite size and the increase in internal strains. Extending the milling time to 150 h results in continuous formation of the FCC-γ phase as well as an increase in peak intensity (Figure 3f). Some authors report the formation of the FCC-γ phase in the Fe-Ni diagram (known as taenite) which coexists with a BCC-α structure called kamacite [31–34].

Table 2. The chemical mixing enthalpy (ΔH_{ij}^{mix}) of binary equiatomic alloys calculated by Miedema's approach [35].

Element	Fe	Ni	B	Si
Fe	-	−2	−26	−35
Ni	-	-	−24	−40
B	-	-	-	−14

Figure 4 shows the evolution of crystallite size and microstrain as a function of milling time. The increase in milling time results in a reduction of the crystallite size and an increase of the lattice strain. During milling time, the Fe crystallite size decreases to 15 nm, with a microstrain of about 0.9% at 50 h. After 10 h of milling, the crystallite size of the Fe (B, Si) solid solution is 15.9 nm, with a microstrain rate of about 0.42%. After 25 h of milling, the Ni crystallite size and the lattice strain are 10 nm and 0.5%, respectively. After 100 h of milling, crystallite sizes and lattice strain levels are close to saturation values. For the BCC (α) phase, the crystallite size reaches a value close to 14.70 nm, with a lattice parameter of about 0.55%. On the other hand, the crystallite size of the FCC (γ) phase reaches a value of about 10.8 nm, with a microstrain rate close to 0.5%. In fact, the multiplication of grain boundaries and the microstrain can increase because of the mechanical distortion and the internal micro-deformation [36]. The steady state of the crystallite size and the lattice strain reached after 100 h of milling could be attributed to the temperature rise of the powder surface during higher milling times [37]. Prolonging the mechanical milling to 150 h, the crystallite size of the BCC and FCC phases reaches values of 13.8 nm and 10.4 nm, respectively. At the same time, the microstrain increases to 0.63% for the BCC (α) and 0.73% for the FCC (γ).

Figure 5 depicts the change of the lattice parameter against milling time. The dissolution of B atoms (R_B = 0.79 Å) [38] and Si atoms (R_{Si} =1.17 Å) [38] into the vacant sites of Fe (R_{Fe} = 1.24 Å) [38] causes an increase in the Fe lattice parameter with increasing milling time. This explains the value of the lattice parameter of the Fe (B, Si) phase, which is a = 2.867 (1) Å after 25 h of milling. With increasing milling time, the lattice parameter of the BCC (α) increases due to the dissolution of Ni in the Fe (B, Si) matrix. However, the Ni atom is quite similar to the iron ones (R_{Ni} = 1.26 Å) [38]. Thus, the lattice parameter increases and reaches a value of a = 2.869 (5) Å at the end of the milling. For the Ni matrix,

the lattice parameter reaches a value of about 3.532 (8) Å; this is due to the expansion of the lattice after 25 h (Figure 5b). After 50 h of milling, the lattice parameter of the FCC (γ) phase is about a = 3.545 (1) Å, and its value increases with increased milling time, reaching a value of a = 3.588 (0) Å at the end of the milling. The increase in the lattice parameter can be explained by the grain expansion due to the increase in the density of dislocations with their characteristic strain fields [39,40].
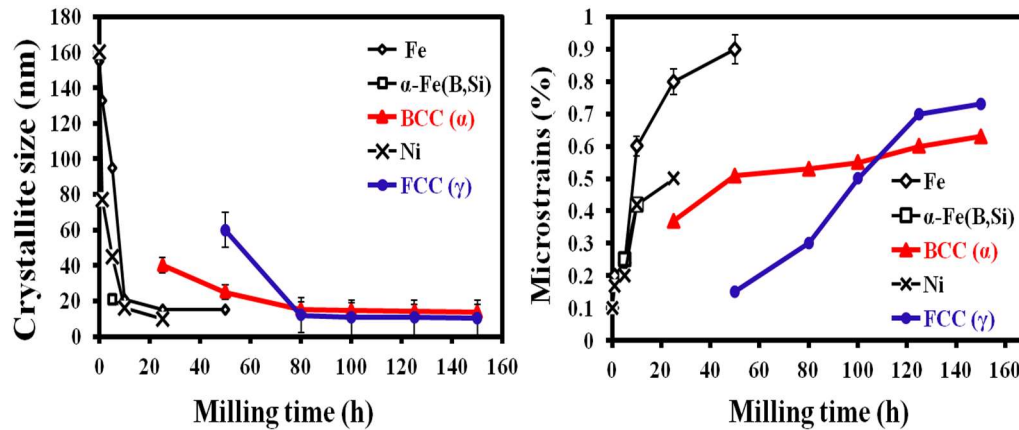

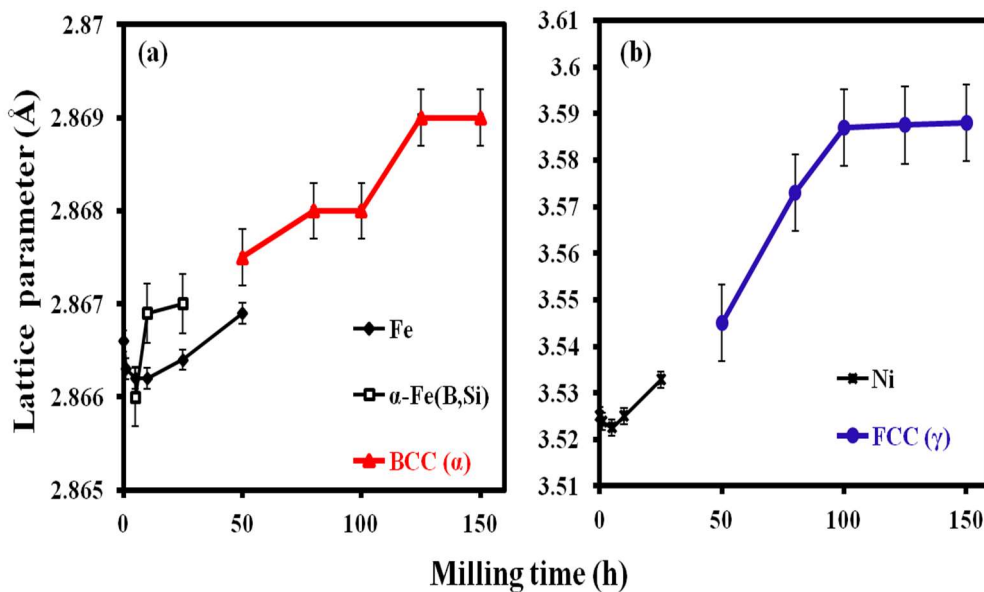**Figure 4.** Microstructure parameters as a function of milling time.

Figure 5. Lattice parameter evolution as a function of the milling time. (**a**) Fe and Fe rich phases, (**b**) Ni and Ni rich phase.

The dislocation densities (ρ_D) of the BCC and FCC phases were determined by applying the Rietveld method. It can be represented by the following equation [41]:

$$\rho_{D=}2\sqrt{3}\frac{<\varepsilon^2>^{1/2}}{Db}, \tag{1}$$

where ε is the lattice strain, D is the crystallite size and b is the Burgers vector. In the case of BCC materials, the cold plastic deformation is caused by the emergence and slip of dislocation on [111] close-packed planes. For the FCC materials, the close-packed plane is [110]. The Burgers vector is represented by $\frac{a}{n}$[hkl], and its intensity is given by

$$b = \frac{a}{n}\sqrt{h2 + k2 + l2} \tag{2}$$

Therefore, the Burger's vector of the BCC phase in direction [111] is represented by $\frac{a}{n}$[111], and its value is $\frac{a\sqrt{3}}{2}$, and for the FCC phase in direction [110] is represented by $\frac{a}{n}$[110], and its value is $\frac{a\sqrt{2}}{2}$, where a is the lattice parameter calculated at each milling time and h, k and l are the Miller indices.

Figure 6 represents the calculated dislocation densities of both the BCC and FCC phases of the alloyed $Fe_{70}Ni_{12}B_{16}Si_2$. For the BCC phase, we can observe a drastic increase of ρ_D from about $0.027 \times 10^{16}/m^2$ to $1.48 \times 10^{16}/m^2$ with increasing milling time from 1 to 80 h. At higher milling time, one can see a slight increase of ρ_D to $1.755 \times 10^{16}/m^2$ after 150 h of milling.
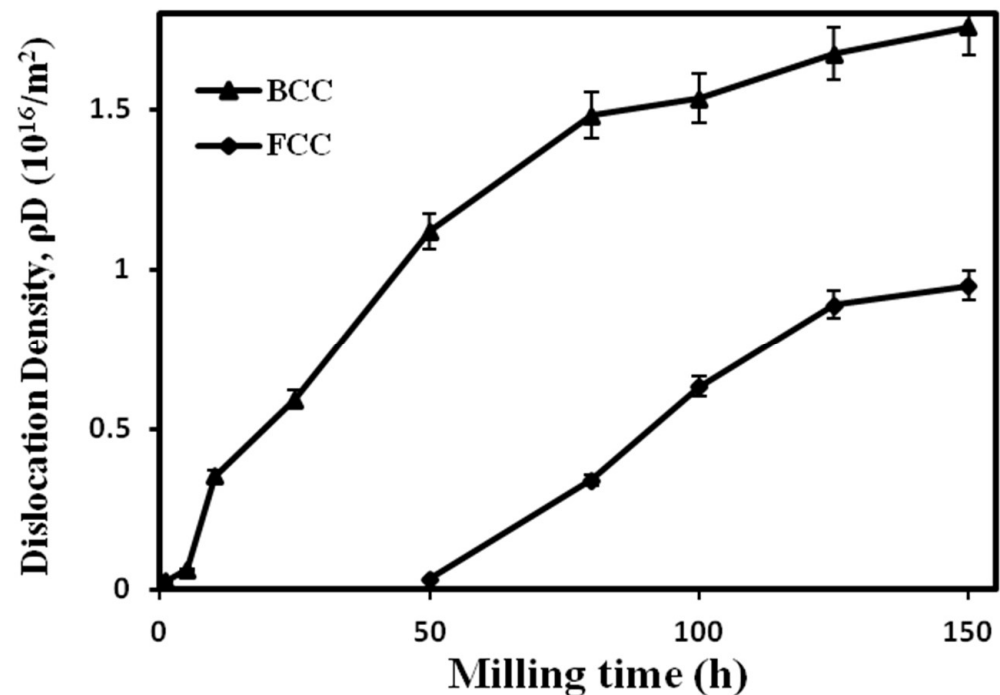

Figure 6. Variation of dislocation density as a function of milling time.

For the FCC phase, a drastic increase is observed from about $0.030 \times 10^{16}/m^2$ at 50 h to $0.89 \times 10^{16}/m^2$ at 125 h. At the end of the milling, the ρ_D slightly increases, reaching $0.95 \times 10^{16}/m^2$.

3.3. Thermal Treatments

Figure 7 shows the DSC results of the sample milled after 150 h under an argon atmosphere; the DSC test was used at a heating rate of 20 K/min. The DSC result reveals an intense exothermic peak appearing around 565 °C, which corresponds to the structural transformation of a large amount of γ-phase to α-phase, as has been discussed in the XRD patterns. At the end of the milling, the α solid solution is decomposed to a α + γ solid solution. The total enthalpy during the transition is found to be 196.40 J/g. The exothermic reaction occurs in the low temperature range and is produced from recovery and strain relaxation [42].

In order to understand the effect of heating on structural and magnetic characterizations, the as-milled sample is annealed at temperatures above the temperature range of the reaction (at 450 and 650 °C for 1 h in argon atmosphere, Figure 8).
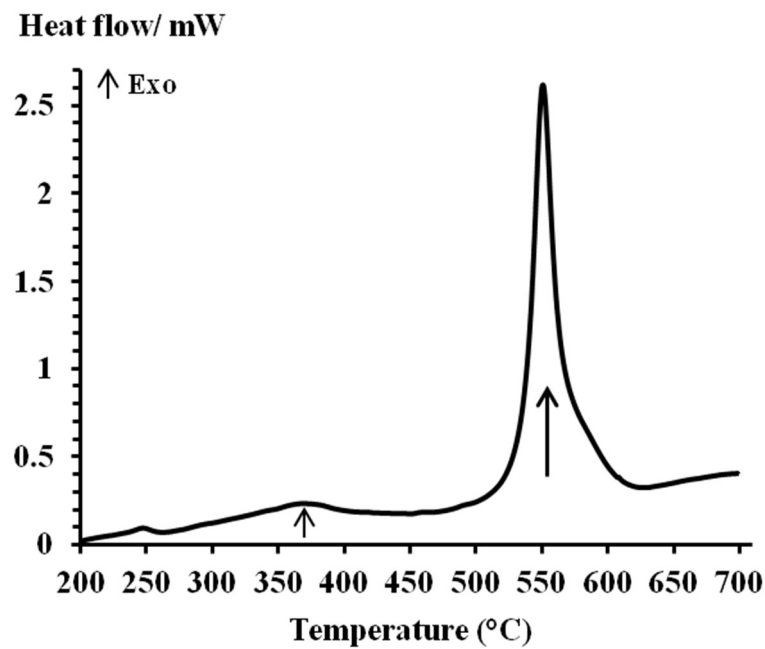
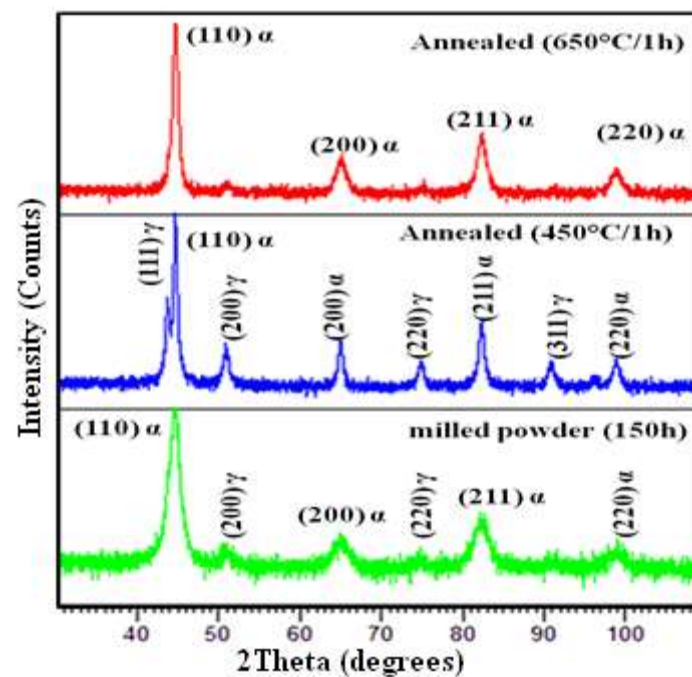**Figure 7.** DSC scan for $Fe_{70}Ni_{12}B_{16}Si_2$ alloy after 150 h of milling (heating rate of 20 °C min^{-1}).

Figure 8. X-ray diffraction patterns of MA $Fe_{70}Ni_{12}B_{16}Si_2$ powders for 150 h of milling obtained after annealing at 450 °C and 650 °C.

XRD analyses were performed. Figure 8 shows the XRD patterns of the as-milled before and after the heat treatment. After the first annealing, one can see that the diffraction peaks of the γ phase become more intensive and sharper (compared with those of as-milled sample with the coexistence of the α phase). We can assume that the original phase ratio was metastable and that the disordered solid solution α-Fe (Ni, B, Si) evolves to ($\alpha + \gamma$) at least below 450 °C. Investigations of the transformation kinetics of the $\alpha \rightarrow \gamma$ phase on annealing can be found in ref. [43]. In our study, a large BCC (α) phase is detected after annealing at 650 °C, with a minor FCC (γ) phase; this can explain the γ to α structure transformation. This indicates that the weight proportion of BCC (α) phase increases after

the second annealing. Thus, the α phase again plays a dominant role, and the proper annealing can promote a transition from FCC (γ) to BCC (α) phase. It was expected that the increased heat temperature would increase the amount of the γ phase; this was not the case in our work. Ahmed and Suryanarayana [44] reported that the γ phase transformed to another α phase with the same crystal structure and lattice parameter. This phase can be the ferrite phase or the stress-induced α′ martensite phase.

Likewise, in order to reach a better understanding of the structural transformation after annealing, we present in Figure 9 the details of the most intense peak (Rietveld refinement), which is the BCC [110]. As we can see, before annealing, the Bragg peak [110] of the sample milled for 150 h is broadened, asymmetrical and seems to be the convolution of two neighboring peaks of the two phases (a major BCC (α) and a minor FCC (γ)). After the first annealing, the BCC [110] peak becomes sharp, and the FCC [111] peak appears and becomes remarkable. After the second annealing, the BCC (α) peak becomes sharper, and the FCC (γ) peak almost disappears.
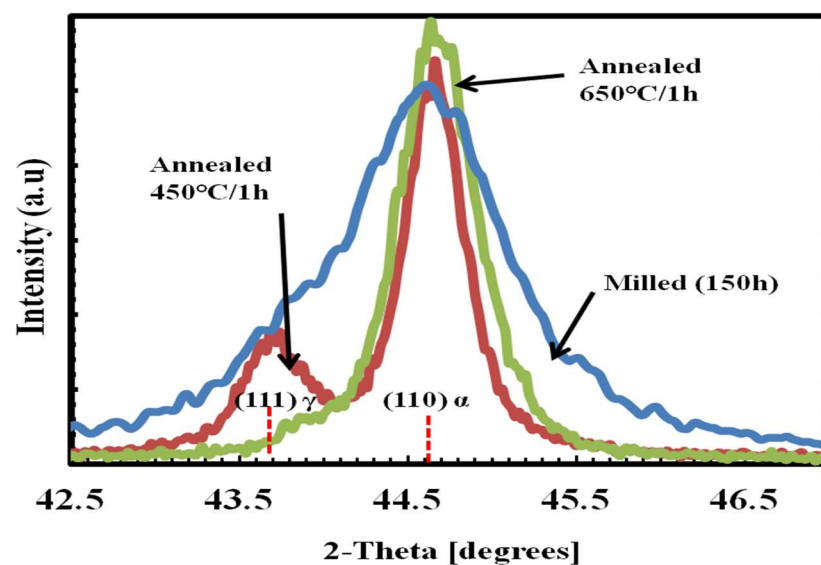

Figure 9. Details of the most intense peak BCC Fe (110) of the of the $Fe_{70}Ni_{12}B_{16}Si_2$ alloy after mechanical alloying and annealing.

As given in Table 3, the percentages and the structural and microstructural parameters of the (α) and γ phases are different in the annealed conditions and the as-milled powders. After annealing at 450 °C for 1 h, the lattice parameter values of the α and γ phases are 2.87 (2) Å and 3.58 (8) Å, respectively. After annealing at 650 °C, the lattice parameter value of the α phase remains unchanged, whereas the lattice parameter of the γ phase decreases. This decrease is in agreement with the shift of the γ peak toward a higher angle, as shown in Figure 8. The crystallite size increases and the lattice strain decreases with annealing [45]. This is due to the reordering of the structure and the decrease of the number of lattice defects. However, the thermal treatments induce a decrease of the internal microstrain as well as nanocrystal growth [46]. The decrease in lattice parameter of the FCC phase may thus be understood in terms of a decrease in crystallographic defects and the reduction of the expansion favored by low density grain boundaries due to the increase in nanocrystal size [46]. This effect is probably compensated in the BCC phase by the thermal favored diffusion of other elements from grain boundaries [46].

3.4. Magnetic Response

In order to study the effect of heat treatment on the magnetic properties of the as-milled powders, the VSM test was performed at room temperature. Figure 10 depicts the hysteresis loop of the samples milled for 150 h and annealed at 450 °C and 650 °C.

It can be stated that the as-milled alloy as well as the annealed sample are semi-hard (1000 < Hc < 40,000 A/m) [47]. Annealing at 450 °C favors alloy magnetic hardening by increasing the coercivity. Likewise, continuous annealing at 650 °C reduces coercivity, favoring semi-hard behavior softening. Thus, magnetic behavior, and specifically semi-hard behavior, can be sifted by designed annealing.

Table 3. Evolution of structural and microstructural proprieties in the investigated $Fe_{70}Ni_{12}B_{16}Si_2$ alloy after mechanical alloying for 150 h and annealing.

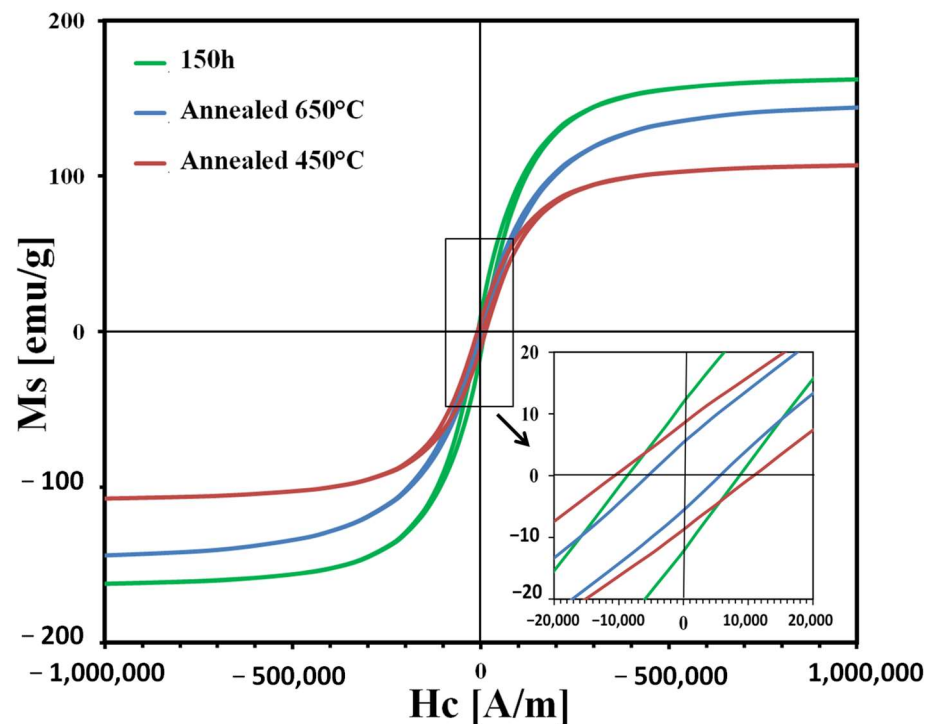| Treatment	BCC α-Phase				FCC γ-Phase			
	Phase Proportion (%)	Lattice Parameter (Å)	Crystallite Size (nm)	Micro-Strain (%)	Phase Proportion (%)	Lattice Parameter (Å)	Crystallite Size (nm)	Micro-Strain (%)
As-milled	91	2.86 (9)	13.76	0.63	9	3.58 (8)	10.44	0.73
Annealing at 450 °C	71	2.87 (0)	38	0.13	29	3.58 (8)	28	0.11
Annealing at 650 °C	96	2.87 (0)	57	0.04	4	3.57 (8)	100	0.05

Figure 10. Magnetic hysteresis plots of 150 h milled $Fe_{70}Ni_{12}B_{16}Si_2$ powders after heat treatment.

Various factors affect the magnetization, such as the chemical composition as well as magnetic atoms' location and their electronic structures. For the present work, and due to the phase transformation during annealing, the total saturation magnetization (M_s) depends on the saturation magnetization of both BCC and FCC phases. Thus, at room temperature, the M_s of $Fe_{70}Ni_{12}B_{16}Si_2$ alloy can be identified as follows [47]:

$$M_{s,total} = V_{FCC} \, M_{s,FCC} + V_{BCC} \, M_{s,BCC}, \tag{3}$$

$$V_{FCC} + V_{BCC} = 1, \tag{4}$$

where the V_{FCC} and V_{BCC} are the relative volume fractions of FCC and BCC phases, respectively, and $M_{s,FCC}$ and $M_{s,BCC}$ are the saturation magnetization of the two phases. Equation (3) can be rewritten as

$$\Delta M_s = (M_{s,BCC} - M_{s,FCC})\, \Delta V_{BCC,} \tag{5}$$

where ΔM_s is the change in saturation magnetization due to the annealing-induced phase transformation and ΔV_{BCC} is the change in the volume fraction of the BCC phase. Therefore, ΔM_s has a close relation with ΔV_{BCC}. This is in agreement with the results taken from the analytical analysis of XRD and the phase proportions calculated by the Rietveld refinement, where the weight proportion of the BCC (α) phase decreases on the first annealing at 450 °C and then increases at 650 °C. Figure 11 shows that the value of M_s also decreases at 450 °C, reaching a value of 109.61 emu/g, and then increasing at 650 °C, reaching a value of 148.27 emu/g. Accordingly, we can conclude that the BCC (α) structure reveals high saturation magnetization compared with the FCC (γ) phase in the $Fe_{70}Ni_{12}B_{16}Si_2$ alloy. Zhang et al. [48] and Huang et al. [49] both reported similar results for $FeCoNi(CuAl)_x$ and $FeCrCoNiAl_x$-alloys. The decrease of the saturation magnetization is also related to the ferrite-to-austenite phase transformation. However, ferritic materials are usually magnetic materials, while austenitic materials are classified as non-magnetic and paramagnetic materials [50]. The increase in M_s after annealing at 650 °C could be attributed to the nucleation of the nanocrystalline ferritic phase.
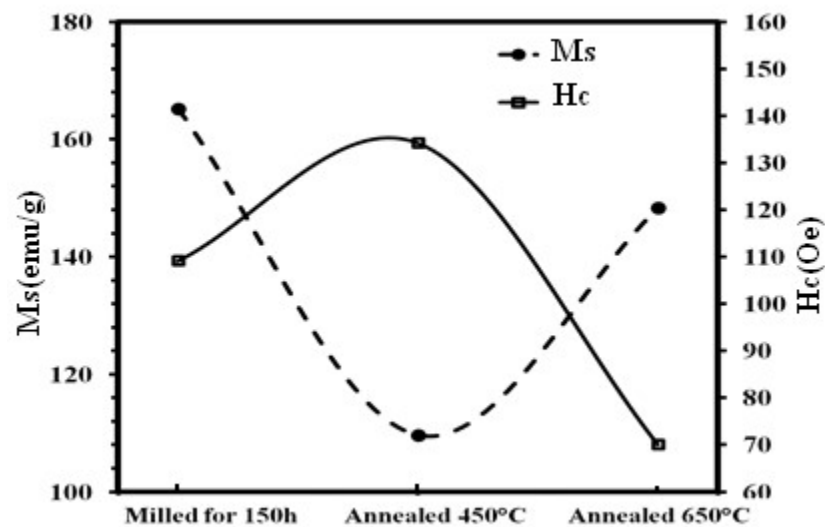

Figure 11. Variation of saturation magnetization (M_s) and coercivity (H_c) of $Fe_{70}Ni_{12}B_{16}Si_2$ powders after milling for 150 h and heat treatment.

Figure 11 also show the coercivity after annealing. H_c increases at 450 °C (134.24 Oe) and decreases after annealing at 650 °C (70.11 Oe). This variation could be explained by the following equation [49]:

$$H_c \propto \frac{\delta_w K_1}{M_s \mu_0 \bar{r}} V_f^{2/3}, \tag{6}$$

It can be noticed that the coercivity is in direct proportion to the volume percentage of the non-magnetic phase (V_f), which is the austenite (γ) phase in our case, in inverse relation to the saturation magnetization (M_s). Where δ_w, μ_0, K_1 and $\bar{r}$ are the domain wall thickness, the vacuum permeability, the magnetocrystalline anisotropy constant and the average magnetic particle size, respectively. After annealing at 450 °C, as discussed above, the saturation magnetization decreases, and the amount of the non-magnetic phase (V_f) increases due to the phase transformation of the BCC ferrite phase to the non-magnetic FCC austenite phase. Thus, the coercivity H_c increases according to Equation (6). On the other hand, with the increase of the saturation magnetization after annealing at 650 °C, the

$Fe_{70}Ni_{12}B_{16}Si_2$ alloy exhibits a remarkable decrease of the non-magnetic phase (V_f), which is the austenite phase. Therefore, the coercivity decreases.

Mishra et al. [51] reported that the reduction in coercivity is due to the increase in crystallite size and the decrease of structural strain after annealing. In our case, this explanation is applicable to the annealing at 650 °C and not to the annealing at 450 °C. Other researchers [52] have found behavior similar to our alloy after annealing at 450 °C. The heat treatment for their $Fe_{42}Ni_{40}B_{18}$ alloy did not show improved magnetic softening, and there was an increase in H_c and a decrease in M_s. Thus, they explain the phenomena by the grain growth that resulted after the annealing, causing the magnetic hardening. Similar studies [23,53] discovered that the increase in coercivity after annealing is caused by the formation of a γ phase.

Figure 12 shows the changes in squareness ratio (M_r/M_s) before and after annealing. The remanence-to-saturation ratio increases from 0.0724 before annealing to 0.0777 after annealing at 450 °C, then decreases to 0.0368 after annealing at 650 °C. Such behavior is quite similar to coercivity changes that have already been observed (Figure 11). This dramatic decrease is probably linked to the release of microstrains and the decrease of the domain wall energy and/or to the phase transition from coexisting BCC + FCC phases at 450 °C to a major BCC phase after annealing at 650 °C. The heat treatment of the powder after annealing at 650 °C improves the magnetic softening of the alloy by decreasing the stress-induced anisotropy. However, the $Fe_{70}Ni_{12}B_{16}Si_2$ alloy powder shows higher saturated magnetization, lower coercivity and lower remanence ratio. A $Fe_{75}Nb_{10}Si_5B_{10}$ alloy milled for 200 h and annealed at 600 K exhibited similar behavior [54]. As a result, applying annealing at 650 °C to the as-milled powder of our alloy shifted the magnetic properties (especially the coercivity and the squareness ratio). It is a viable alternative to the addition of a minor amount of other elements [55].
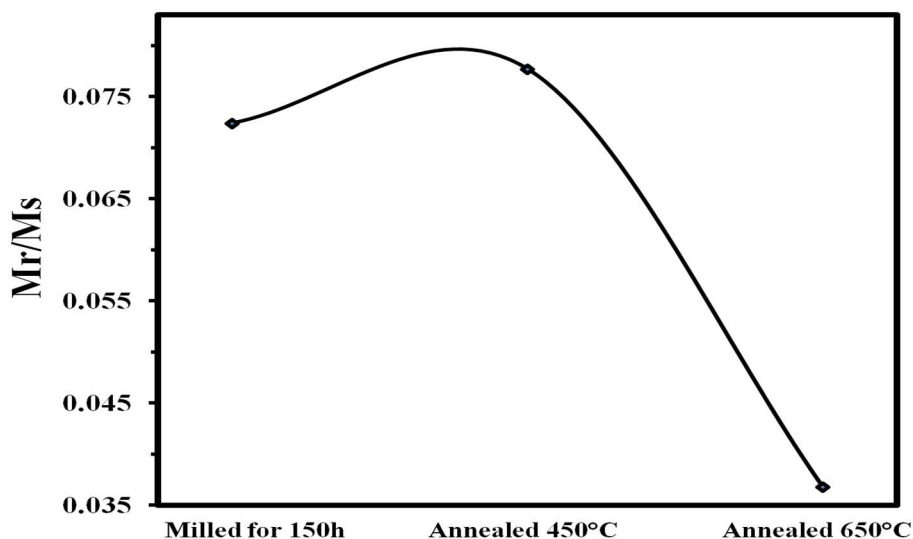

Figure 12. Values of the squareness ratio (M_r/M_s) of $Fe_{70}Ni_{12}B_{16}Si_2$ powders after milling for 150 h and heat treatment.

4. Conclusions

A nanocrystalline $Fe_{70}Ni_{12}B_{16}Si_2$ powdered alloy was successfully synthesized through a mechanical alloying process. The following conclusions were obtained.

Milling time has an important effect on the formation of phases, crystallite size and microstrain. The formation of nanocrystalline solid solutions was obtained after milling. The presence of a major BCC phase (crystalline size 13 nm) and a minor FCC phase (10 nm crystalline phase) in the final powder milled for 150 h was observed.

A partial solid state $\alpha \rightarrow \gamma$ transformation after annealing at 450 °C was observed, coupled with a decrease in the saturation magnetization and an increase in the coercivity

and the remanence ratio. From the results, the alloy may be classified, when as-milled and annealed at 450 °C, as a semi-hard alloy.

A $\gamma \rightarrow \alpha$ transformation after annealing at 650 °C resulted in obtaining a major ferromagnetic α phase, accompanied by an increase in the saturation magnetization (up to 148.27 emu/g) and a dramatic decrease in both the coercivity, of about 70 Oe, and the remanence ratio, of about 0.036. As a result, semi-hard behavior was shifted. Thus, magnetic properties are strongly affected by the phase transformation after annealing.

Author Contributions: Conceptualization, M.K., M.C. and L.E.; methodology, J.S. and L.E.; formal analysis, K.Z. and N.L.-I.; data curation, J.S. and N.L.-I.; writing—original draft preparation, K.Z. and J.-J.S.; supervision, J.-J.S., M.K. and M.C. All authors have read and agreed to the published version of the manuscript.

Institutional Review Board Statement: Not applicable.

Informed Consent Statement: Not applicable.

Data Availability Statement: Data can be requested from the authors.

Conflicts of Interest: The authors declare no conflict of interest.

References

1. Kezrane, M.; Guittoum, A.; Hemmous, M.; Lamrani, S.; Bourzami, A.; Weber, W. Elaboration, Microstructure, and Magnetic Properties of Nanocrystalline $Fe_{90}Ni_{10}$ Powders. *J. Supercond. Nov. Magn.* **2015**, *28*, 2473–2481. [CrossRef]
2. Suryanarayana, C.; Al-Joubori, A.A.; Wang, Z. Nanostructured Materials and Nanocomposites by Mechanical Alloying: An Overview. *Met. Mater. Int.* **2021**, 1–13. [CrossRef]
3. Sunol, J.J.; Gonzalez, A.; Escoda, L. Comparison of Fe-Ni based alloys prepared by ball milling and rapid solidification. *J. Mater. Sci.* **2004**, *39*, 5147–5150. [CrossRef]
4. García-Garrido, C.; Sepúlveda-Ferrer, R.; Salvo, C.; García-Domínguez, L.; Pérez-Pozo, L.; Lloreda-Jurado, P.J.; Chicardi, E. Effect of Milling Parameters on the Development of a Nanostructured FCC–$TiNb_{15}Mn$ Alloy via High-Energy Ball Milling. *Metals* **2021**, *11*, 1225. [CrossRef]
5. Suryanarayana, C. Mechanical alloying: A novel technique to synthesize advanced materials. *Research* **2019**, *4219812*, 1–17. [CrossRef]
6. Helle, S.; Pedron, M.; Assouli, B.; Davis, B.; Guay, D.; Roué, L. Structure and high-temperature oxidation behaviour of Cu–Ni–Fe alloys prepared by high-energy ball milling for application as inert anodes in aluminium electrolysis. *Corros. Sci.* **2010**, *52*, 3348–3355. [CrossRef]
7. Mondal, B.N.; Basumallick, A.; Chattopadhyay, P.P. Effect of isothermal treatments on the magnetic behavior of nanocrystalline Cu–Ni–Fe alloy prepared by mechanical alloying. *J. Magn. Magn. Mater.* **2007**, *309*, 290–294. [CrossRef]
8. Chater, R.; Bououdina, M.; Chaanbi, D.; Abbas, H. Synthesis and magnetization studies of nanopowder $Fe_{70}Ni_{20}Cr_{10}$ alloys prepared by high energy milling. *J. Solid State Chem.* **2013**, *201*, 317–323. [CrossRef]
9. Paul, A.A.; Rathi, A.; Thotakura, G.V.; Jayaraman, T.V. Influence of milling atmosphere on the structure and magnetic properties of mechanically alloyed $Fe_{40}Co_{30}Ni_{30}$. *Mater. Chem. Phys.* **2021**, *258*, 123897. [CrossRef]
10. Saravanan, T.T.; Kumaran, S.; Rao, T.S. Structural evolution and magnetic properties of mechanically alloyed metastable Fe–Ni–Zr–B system. *Mater. Lett.* **2009**, *63*, 780–782. [CrossRef]
11. Panigrahi, M.; Avar, B. Influence of mechanical alloying on structural, thermal, and magnetic properties of $Fe_{50}Ni_{10}Co_{10}Ti_{10}B_{20}$ high entropy soft magnetic alloy. *J. Mater. Sci. Mater. Electron.* **2021**, *32*, 21124–21134. [CrossRef]
12. Suñol, J.J. Structural and Thermal Study of Fe-Ni-Si-B Powders Prepared by Mechanical Alloying. In *Materials Science Forum*; Trans Tech Publ. Ltd.: Stafa-Zurich, Switzerland, 1998; Volume 269, pp. 503–512.
13. Gupta, A.; Habibi, S.; Principi, G. Study of short-range order in Fe–Ni–Si–B amorphous alloys. *Mater. Sci. Eng. A* **2001**, *304*, 1058–1061. [CrossRef]
14. Varga, R.; Gamcova, J.; Klein, P.; Kovac, J.; Zhukov, A. Tailoring the switching field dependence on external parameters in magnetic microwires. *IEEE Trans. Magn.* **2012**, *49*, 30–33. [CrossRef]
15. Wang, J.G.; Zhao, H.; Xie, C.X.; Chang, C.T.; Zhou, S.M.; Feng, J.Q.; Li, W.H. In-situ synthesis of nanocrystalline soft magnetic Fe-Ni-Si-B alloy. *J. Alloys Compd.* **2019**, *790*, 524–528. [CrossRef]

16. Liu, T.; Wang, A.; Zhao, C.; Yue, S.; Wang, X.; Liu, C.T. Compositional design and crystallization mechanism of High Bs nanocrystalline alloys. *Mater. Res. Bull.* **2019**, *112*, 323–330. [CrossRef]
17. Liu, C.; Inoue, A.; Kong, F.L.; Zanaeva, E.; Bazlov, A.; Churyumov, A.; Shull, R.D. Fe-B-Si-C-Cu amorphous and nanocrystalline alloys with ultrahigh hardness and enhanced soft magnetic properties. *J. Non-Cryst. Solids* **2021**, *554*, 120606. [CrossRef]
18. Lutterotti, L. *Maud Program*; Int. Union of Crystallography, CPD Newsletter: Chester, UK, 2000; Volume 24.
19. Young, R.A.; Wiles, D.B. Profile shape functions in Rietveld refinements. *J. Appl. Crystallogr.* **1982**, *15*, 430–438. [CrossRef]
20. Dutta, H.; Pradhan, S.K.; De, M. Microstructural evolution on ball-milling elemental blends of Ni, Al and Ti by Rietveld's method. *Mater. Chem. Phys.* **2000**, *74*, 167–176. [CrossRef]
21. Lutterotti, L.; Scardi, P.; Maistrelli, P. LSI-a computer program for simultaneous refinement of material structure and microstructure. *J. Appl. Crystallogr.* **1992**, *25*, 459–462. [CrossRef]
22. Rietveld, H.M. Line profiles of neutron powder-diffraction peaks for structure refinement. *Acta Crystallogr.* **1967**, *22*, 151–152. [CrossRef]
23. Abbasi, S.; Eslamizadeh, H.; Raanaei, H. Study of synthesis, structural and magnetic properties of nanostructured $(Fe_{67}Ni_{33})_{70}Ti_{10}B_{20}$ alloy. *J. Magn. Magn. Mater.* **2018**, *451*, 780–786. [CrossRef]
24. Hadef, F.; Otmani, A.; Djekoun, A.; Grenèche, J.M. Investigation of mechanosynthesized $Fe_{50}Ni_{40}Al_{10}$ powders. *J. Magn. Magn. Mater.* **2013**, *343*, 214–220. [CrossRef]
25. Baghbaderani, H.A.; Sharafi, S.; Chermahini, M.D. Investigation of nanostructure formation mechanism and magnetic properties in $Fe_{45}Co_{45}Ni_{10}$ system synthesized by mechanical alloying. *Powder Technol.* **2012**, *230*, 241–246. [CrossRef]
26. Raanaei, H.; Eskandari, H.; Mohammad-Hosseini, V. Structural and magnetic properties of nanocrystalline Fe–Co–Ni alloy processed by mechanical alloying. *J. Magn. Magn. Mater.* **2016**, *398*, 190–195. [CrossRef]
27. Luo, H.; Xin, Y.; Ma, Y.; Liu, B.; Meng, F.; Liu, H.; Wu, G. FCC Fe_2NiSi prepared by mechanical alloying and stabilization effect of $L_{21}B$ disorder on BCC Heusler structure. *J. Magn. Magn. Mater.* **2016**, *419*, 485–489. [CrossRef]
28. Raanaei, H.; Fakhraee, M. Synthesis and characterization of nanocrystalline Co-Fe-Nb-Ta-B alloy. *J. Magn. Magn. Mater.* **2017**, *438*, 144–151. [CrossRef]
29. Azzaza, S.; Hadef, F.; Chater, R.; Abbas, H.; Zerniz, N.; Benmoussa, A.; Bououdina, M. Structural and Magnetic Properties of Mechanically Alloyed and Oxidized Fe-Based Powder Mixtures. *J. Supercond. Nov. Magn.* **2016**, *29*, 1583–1592. [CrossRef]
30. Gheisari, K.; Javadpour, S.; Oh, J.T.; Ghaffari, M. The effect of milling speed on the structural properties of mechanically alloyed Fe–45% Ni powders. *J. Alloys Compd.* **2009**, *472*, 416–420. [CrossRef]
31. Baldokhin, Y.V.; Tcherdyntsev, V.V.; Kaloshkin, S.D.; Kochetov, G.A.; Pustov, Y.A. Transformations and fine magnetic structure of mechanically alloyed Fe–Ni alloys. *J. Magn. Magn. Mater.* **1999**, *203*, 313–315. [CrossRef]
32. Hong, L.B.; Fultz, B. Two-phase coexistence in Fe–Ni alloys synthesized by ball milling. *J. Appl. Phys.* **1996**, *79*, 3946–3955. [CrossRef]
33. Djekoun, A.; Otmani, A.; Bouzabata, B.; Bechiri, L.; Randrianantoandro, N.; Greneche, J.M. Synthesis and characterization of high-energy ball milled nanostructured $Fe_{50}Ni_{50}$. *Catal. Today* **2006**, *113*, 235–239. [CrossRef]
34. Kuhrt, C.; Schultz, L. Formation and magnetic properties of nanocrystalline mechanic ally alloyed Fe-Co and Fe-Ni. *J. Appl. Phys.* **1993**, *73*, 6588–6590. [CrossRef]
35. Takeuchi, A.; Inoue, A. Classification of bulk metallic glasses by atomic size difference, heat of mixing and period of constituent elements and its application to characterization of the main alloying element. *Mater. Trans.* **2005**, *46*, 2817–2829. [CrossRef]
36. Zaara, K.; Chemingui, M.; Optasanu, V.; Khitouni, M. Solid solution evolution during mechanical alloying in Cu-Nb-Al compounds. *Int. J. Miner. Metall. Mater.* **2019**, *26*, 1129–1139. [CrossRef]
37. Slimi, M.; Saurina, J.; Suñol, J.J.; Escoda, L.; Farid, M.; Greneche, J.M.; Khitouni, M. Mössbauer and X-ray studies of mechanically alloyed $Fe_{60}Ni_{30}Cr_{10}$ prepared by high energy ball milling. *Adv. Powder Technol.* **2016**, *27*, 1618–1624. [CrossRef]
38. Rahm, M.; Hoffman, R.; Aschroft, N.W. Atomic and ionic radii of elements 1–96. *Chem. Eur. J.* **2016**, *22*, 14625–14632. [CrossRef] [PubMed]
39. Carrillo, A.; Daza, J.; Saurina, J.; Escoda, L.; Suñol, J.J. Structural, Thermal and Magnetic Analysis of $Fe_{75}Co_{10}Nb_6B_9$ and $Fe_{65}Co_{20}Nb_6B_9$ Nanostructured Alloys. *Materials* **2021**, *14*, 4542. [CrossRef] [PubMed]
40. Mhadhbi, M.; Khitouni, M.; Azabou, M.; Kolsi, A. Characterization of Al and Fe nanosized powders synthesized by high energy mechanical milling. *Mater. Charact.* **2008**, *59*, 944–950. [CrossRef]
41. Pippan, R.; Wetscher, F.; Hafok, M.; Vorhauer, A.; Sabirov, I. The limits of refinement by severe plastic deformation. *Adv. Eng. Mater.* **2006**, *8*, 1046–1056. [CrossRef]
42. Carrillo, A.; Saurina, J.; Escoda, L.; Suñol, J.J. Fe-X-B-Cu (X = Nb, NiZr) alloys produced by mechanical alloying: Influence of milling device. *Metals* **2021**, *11*, 379. [CrossRef]
43. Al-Joubori, A.A.; Suryanarayana, C. Synthesis and stability of the austenite phase in mechanically alloyed Fe–Cr–Ni alloys. *Mater. Lett.* **2017**, *187*, 140–143. [CrossRef]
44. Al-Joubori, A.A.; Suryanarayana, C. Synthesis of austenitic stainless steel powder alloys by mechanical alloying. *J. Mater. Sci.* **2017**, *52*, 11919–11932. [CrossRef]
45. Gheiratmand, T.; Hosseini, H.M. Synthesis of FeNiCoTi Powder Alloy by Mechanical Alloying and Investigation of Magnetic and Shape Memory Properties. *J. Supercond. Nov. Magn.* **2012**, *25*, 1893–1899. [CrossRef]

46. Karimi, L.; Shokrollahi, H.; Karimi, Z.; Mohammadi, M. Improvement of magnetic properties of nanostructured $Ni_{79}Fe_{16}Mo_5$ alloyed powders by a suitable heat treatment. *Adv. Powder Technol.* **2013**, *24*, 653–658. [CrossRef]

47. Coey, J.M.D. Hard magnetic materials: A perspective. *IEEE Trans. Magn.* **2011**, *47*, 4671–4681. [CrossRef]

48. Zhang, Q.; Xu, H.; Tan, X.H.; Hou, X.L.; Wu, S.W.; Tan, G.S.; Yu, L.Y. The effects of phase constitution on magnetic and mechanical properties of FeCoNi (CuAl) x (x = 0–1.2) high-entropy alloys. *J. Alloys Compd.* **2017**, *693*, 1061–1067. [CrossRef]

49. Huang, S.; Li, W.; Li, X.; Schönecker, S.; Bergqvist, L.; Holmström, E.; Vitos, L. Mechanism of magnetic transition in FeCrCoNi-based high entropy alloys. *Mater. Des.* **2016**, *103*, 71–74. [CrossRef]

50. Amini, R.; Shokrollahi, H.; Salahinejad, E.; Hadianfard, M.J.; Marasi, M.; Sritharan, T. Microstructural, thermal and magnetic properties of amorphous/nanocrystalline FeCrMnN alloys prepared by mechanical alloying and subsequent heat treatment. *J. Alloys Compd.* **2009**, *480*, 617–624. [CrossRef]

51. Mishra, R.K.; Shahi, R.R. Phase evolution and magnetic characteristics of TiFeNiCr and TiFeNiCrM (M = Mn, Co) high entropy alloys. *J. Magn. Magn. Mater.* **2017**, *442*, 218–223. [CrossRef]

52. Du, S.W.; Ramanujan, R.V. Mechanical alloying of Fe–Ni based nanostructured magnetic materials. *J. Magn. Magn. Mater.* **2005**, *292*, 286–298. [CrossRef]

53. Nowroozi, M.A.; Shokrollahi, H. The effects of milling time and heat treatment on the micro-structural and magnetic behavior of $Fe_{42}Ni_{28}Zr_8Ta_2B_{10}C_{10}$ synthesized by mechanical alloying. *J. Magn. Magn. Mater.* **2013**, *335*, 53–58. [CrossRef]

54. Suñol, J.J.; Escoda, L.; Fort, J.; Pérez, J.; Pujol, T. Structural and magnetic properties of a nanocrystalline $Fe_{75}Nb_{10}Si_5B_{10}$ alloy produced by mechanical alloying. *Mater. Lett.* **2008**, *62*, 1673–1676. [CrossRef]

55. Jia, X.; Li, Y.; Wu, L.; Zhang, W. A study on the role of Ni content on structure and properties of Fe–Ni–Si–B–P–Cu nanocrystalline alloys. *J. Alloys Compd.* **2020**, *822*, 152784. [CrossRef]